JOURNAL OF SPACECRAFT AND ROCKETS
Vol. 47, No. 4, July–August 2010

Formation Control at the Sun–Earth L_2 Libration Point Using Solar Radiation Pressure

Kamran Shahid* and K. D. Kumar†
Ryerson University, Toronto, Ontario M5B 2K3, Canada

DOI: 10.2514/1.47342

In this paper the use of solar radiation pressure for spacecraft formation flying at the L_2 sun–Earth/moon collinear libration point is presented. The system consisting of a leader and a follower satellite is considered. The leader satellite is assumed to be in a fixed halo trajectory and the follower satellite position relative to the leader satellite is controlled using two angles and area; these are varied based on a higher-order sliding-mode control technique to achieve the desired formation control. The stability of the proposed controller is established using Lyapunov theory. The performance of the proposed controller is tested through numerical simulation of the governing nonlinear equations of motion and is applied for both formationkeeping and formation reconfiguration in the elliptical restricted three-body problem. The effects of initial state errors, nonnatural formations and optical solar sail material degradation are considered. The numerical results demonstrate the effectiveness of the proposed control technique for precise satellite formation flying using solar radiation pressure at the L_2 libration point. Furthermore, control inputs on the order of 10 deg and 4 m^2 for area change are sufficient to control formation reconfiguration changes as large as 25 km.

Nomenclature

A_i = amplitude in the i direction, dimensionless
A_0 = solar sail reference area, m^2
B_f, B_b = front and backside non-Lambertian coefficients
b_i = derived optical coefficients, dimensionless
C_{L_2} = L_2 linearization constant, dimensionless
D = distance from sun to Earth/moon system, dimensionless
d_{ij} = distance from spacecraft i to body j, dimensionless
k = ratio of x and y amplitudes, dimensionless
l_2 = collinear point location, km
m_1, m_2, m = mass of the sun, Earth/moon system, and satellite, kg
$\hat{n}$ = solar sail normal vector
p_0 = nominal solar radiation pressure force, N
Q_0, q = characteristic solar sail acceleration and change in solar sail acceleration, dimensionless
$\mathbf{r}$, $\mathbf{r}_I$ = position vector of satellite expressed in L_2 and inertial frame, dimensionless
r_{12} = distance from sun to Earth/moon system, km
$\mathbf{s}$ = sun vector
s, ρ = specular and reflection coefficients
T, U = spacecraft kinetic and potential energy
t = time, dimensionless
u = control input
X, X_d = follower spacecraft actual and desired relative state vector, dimensionless
β = solar sail lightness number, dimensionless
γ = collinear point location, dimensionless
Δa, ϕ, α = area change and solar sail orientation angles, dimensionless
δ = switching boundary layer, dimensionless
ε_f, ε_b = front and backside emission coefficients
ϵ_i = ellipsoid region, dimensionless
θ = true anomaly, dimensionless
λ, C, η, k_i = control gains, dimensionless
μ = mass ratio $m_2/(m_1+m_2)$, dimensionless
ν_{xy}, ν_z = in-plane and out-of-plane eigenvalues
Σ = half-life solar radiation dose, years
φ, ε = azimuth and elevation angles, dimensionless
ψ = phase angle, dimensionless

I. Introduction

SPACECRAFT formation flying is the concept of distributing the functionality of large spacecraft among smaller, less expensive, cooperative spacecraft. This approach has several advantages including simpler design, higher redundancy, lower production cost, and enhanced mission flexibility. Spacecraft formation flying also has the potential to enhance space-based imaging interferometry missions by distributing the optical elements of the interferometer over a system of multiple spacecraft flying in precise formation. This approach allows for longer and adjustable observation baselines and larger light-collecting areas. Formation-flying interferometry missions that are currently under development include Darwin [1], the Stellar Imager [2], and the Terrestrial Planet Finder [3]. These formation-flying missions are all designed to be located at the L_2 sun–Earth/moon Lagrange point.

The Lagrangian points are the five stationary solutions to the circular restricted three-body problem (CR3BP). The CR3BP deals with the motion of an infinitesimal body in the gravitational field of two significantly larger primary bodies that are in a circular orbit about their mass center. The Lagrange points L_1, L_2, and L_3 are collinear with the sun–Earth/moon line, whereas L_4 and L_5 points form an equilateral triangle with the sun–Earth/moon line. A primary benefit of operating formation-flying interferometry missions near the Lagrange points is that spacecraft near these points have an almost unobstructed view of celestial objects and are not affected by geomagnetic and atmospheric forces. The L_2 point has the additional advantage that the sun, Earth, and moon all lie in the same direction, thereby reducing the interference from these bodies.

The practical implementation of formation flying at L_2 requires the precise control of the relative positions and orientations of the formation satellites. Infeld et al. [4] addressed both issues of orbit design and formation control by treating the formation-flying

---

Received 24 September 2009; revision received 22 March 2010; accepted for publication 29 March 2010.

[*] Graduate Candidate, Department of Aerospace Engineering, 350 Victoria Street; kshahid@ryerson.ca.

[†] Associate Professor and Canada Research Chair in Space Systems, Department of Aerospace Engineering, 350 Victoria Street; krishnadevkumar@yahoo.com.

problem as a multi-agent, nonlinear, constrained optimal control problem. Fuel expenditure was also minimized in this study. A discrete control method was investigated by Pernicka et al. [5] to maintain a two satellite formation using differential correction methods. Marchand and Howell [6] used a linear quadratic regulator and feedback linearization to accomplish formation-flying control. The effectiveness of the control methods was tested in the CR3BP and in the ephemeris model. Adaptive control that compensated for the unknown mass of the follower satellite was proposed by Wong and Kapila [7]. Here, the controller was designed to compensate for the lack of the follower spacecraft relative velocity measurements. Luquette and Sanner [8] developed a nonlinear control method based on feedback linearization to develop a six-degree-of-freedom control algorithm for maintaining the relative position and attitude of a spacecraft within a formation. Gurfil et al. [9] used a nonlinear adaptive neural control methodology for precision control of deep-space spacecraft formation flying in the CR3BP. Here, the leader spacecraft was not confined to the vicinity of a libration point. In all of these studies, the required control inputs are generated by conventional low thrust propulsion systems. At the libration points, the magnitude of the required thrust inputs for satellite control is usually of the same order of magnitude as the perturbing force produced by solar radiation pressure. This observation has led to an interest in using solar radiation pressure for satellite formation control at the libration points.

Solar sailing is an emerging propulsion technology that has the potential to become a viable alternative to chemical propulsion systems. In the CR3BP environment, solar radiation pressure can be used to generate artificial libration points. McInnes [10] showed that solar radiation pressure shifts libration points Earthward at L_2 and sunward at L_1. Few researchers have investigated the use of solar radiation pressure to control a satellite trajectory in the vicinity of the libration points. Bookless and McInnes [11] investigated the use of solar radiation pressure to provide stationkeeping at a quasi0periodic orbits around L_2. Here, a linear quadratic regulator was used to vary the solar sail area and solar sail pitch and roll angles to affect the resultant solar radiation pressure force. The reconfiguration of an L_1 satellite formation was examined by Li and Williams [12]. Linearized dynamics were used to determine the sail orientation angle needed to change the trajectory of the follower satellite. Nonlinear feedback control for solar sailing spacecraft has not been developed. A nonlinear control system can provide improved control system performance by compensating for system nonlinearities and accommodating model uncertainties.

The development of feedback control for a solar radiation pressure controlled satellite deals with the nonaffine control inputs. In an affine system, the control input appears linearly in the state equation. However, in a solar radiation pressure (SRP) model, the resultant forces are a function of the control inputs making the system nonaffine. An approach to resolving this problem is to transform a nonlinear state equation that is nonaffine in u into an augmented state space model that is linear in $\dot{u}$. The time derivative of u is then used as the new control input. This approach has been used by several researchers. Boskovic et al. [13] developed an adaptive tracking control algorithms for a class of nonaffine flight control models. Hovakimyan et al. [14] developed a method for approximate dynamic inversion of nonaffine-in-control systems using time-scale separation. The developed control input is determined as the solution of fast system dynamics and is shown to asymptotically stabilize the original nonaffine system. In this study, higher-order sliding-mode control (HOSMC) is used to address the nonaffine SRP control inputs. Higher-order sliding-mode was originally developed by Levant [15] to contend with the chattering problem in sliding-mode control. This method features a bounded continuous control input with discontinuities only in the control derivative. The application of higher-order sliding mode to aircraft pitch control was also presented by Levant et al. [16]. Bartolini et al. [17] extended the higher-order sliding-mode concept and applied it to multi-input nonlinear uncertain systems. Other applications of higher-order sliding mode include aircraft formation-flight control [18], missile interceptor guidance, [19], and blood glucose regulation [20]. It will be shown that the higher-order sliding-mode technique can be adopted to address the problem of nonaffine SRP control inputs.

Some researchers have investigated the use of solar radiation pressure for formation-flying control. Li and Williams [12] proposed the use of solar radiation pressure for formation configuration at the L_1 point; however, this approach used open-loop control based on the linearized dynamics. In this work the leader satellite is also required to change its orientation to produce the desired solar radiation pressure force. Bookless and McInnes [11] did use linear feedback using solar radiation pressure, but this was only for the stationkeeping control of one satellite orbiting the L_2 point, and not for formation-flying control. These studies have not accounted for external disturbances and have based their work on a simplified solar radiation pressure model. With a view to overcome these limitations, this paper investigates the use of solar radiation pressure for formation-flying control at the L_2 libration point using nonlinear higher-order sliding-mode control.

The main contributions of this study relative to other works include the accommodation of the nonaffine SRP control input by using nonlinear higher-order sliding-mode control. A nonlinear solar radiation pressure controller for L_2 satellite formation flying has not been investigated in the existing literature. The controller is developed in the simplified circular restricted three-body problem but is tested in the elliptical restricted three-body problem. A nonideal solar sail optical model is also used, and the effects of the optical degradation of the solar sail material on formation flying are examined.

II. System Model

The elliptic restricted three-body problem (ER3BP) deals with the motion of an infinitesimal spacecraft mass m in the gravitational field of two primary bodies m_1 and m_2. Here, m_1 is the mass of the sun and m_2 is the combined mass of the Earth and moon. The sun–Earth/moon systems revolves about its center of mass in an elliptical orbit (see Fig. 1). The mass of the satellite is assumed to be significantly smaller than the masses of the primary bodies, $m \ll m_1$ and $m \ll m_2$. Thus, the satellite does not influence the motion of the two primaries. The equations of motion of the satellite m are expressed in nondimensional units by defining the mean Earth–sun distance, the mean angular rate of the finite bodies about the barycenter and the

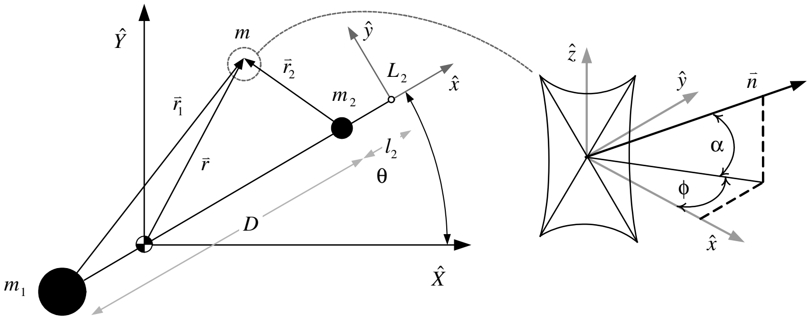

Fig. 1 Geometry of the three-body problem and solar sail normal orientation.

sum of the masses of the two finite bodies as unity. By defining $\mu \triangleq m_2/(m_1 + m_2)$, m_1 is located at $(-\mu, 0, 0)$ and m_2 is located at $[(1-\mu), 0, 0]$. The location of the L_2 collinear point varies, since the Earth–sun distance D varies. However, the ratio $l_2/D = \gamma$ remains constant. The position vector of a satellite, an infinitesimal mass, expressed in the L_2 frame, but relative to the large mass $(1-\mu)$ is

$$\mathbf{r} = [(1+\gamma)D + x]\hat{\imath} + y\hat{\jmath} + z\hat{k} \tag{1}$$

Differentiation of the preceding expression yields the velocity vector relative to the larger primary:

$$\dot{\mathbf{r}} = [(1+\gamma)\dot{D} + \dot{x} - \dot{\theta}y]\hat{\imath} + [\theta[(1+\gamma)D + x] + \dot{y}]\hat{\jmath} + \dot{z}\,\hat{k} \tag{2}$$

The kinetic energy of the satellite body is

$$T = \frac{m}{2}\dot{\mathbf{r}} \cdot \dot{\mathbf{r}} \tag{3}$$

and the effective potential energy for motion of the satellite relative to the larger primary is given by [21]

$$U = -\frac{(1-\mu)}{r_1} - \mu\left[\frac{1}{r_2} - \frac{(1+\gamma)D + x}{D^2}\right] \tag{4}$$

where $r_1^2 = [x + (1+\gamma)D]^2 + y^2 + z^2$ and $r_2^2 = [\gamma D + x]^2 + y^2 + z^2$.

A. Equations of Motion

The generalized coordinates for the Lagrange formulation are $q_k = [x \quad y \quad z]^T$. Using Eqs. (2–4) and (38) with the Lagrange equations

$$\frac{\mathrm{d}}{\mathrm{d}t}\left(\frac{\partial T}{\partial \dot{q}_k}\right) - \frac{\partial T}{\partial q_k} + \frac{\partial U}{\partial q_k} = \vec{F} \cdot \frac{\partial \vec{r}}{\partial q_k} \tag{5}$$

yields the equations of motion of a single satellite relative to the L_1 collinear point. Consider a satellite formation consisting of a leader and follower satellite. The dynamics of the follower satellite relative to the leader satellite are expressed as $\ddot{\mathbf{r}} = \ddot{\mathbf{r}}_F - \ddot{\mathbf{r}}_L$. Redefining the coordinates $[x \quad y \quad z]^T$ as relative coordinates (i.e., $x = x_F - x_L$, $y = y_F - y_L$, $z = z_F - z_L$) gives the ER3BP SFF equations of motion:

$$\begin{aligned}\ddot{x} - 2\dot{y}\,\dot{\theta} - y\ddot{\theta} - x\dot{\theta}^2 &= -(1-\mu)\left[\frac{x}{d_{FS}^3} + [x_L + (1+\gamma)D]\left(\frac{1}{d_{FS}^3} - \frac{1}{d_{LS}^3}\right)\right] \\ &\quad - \mu\left[\frac{x}{d_{FE}^3} + [x_L + \gamma D]\left(\frac{1}{d_{FE}^3} - \frac{1}{d_{LE}^3}\right)\right] + f_{Fx} - f_{Lx}\end{aligned} \tag{6}$$

$$\begin{aligned}\ddot{y} - y\dot{\theta}^2 + 2\dot{\theta}\,\dot{x} + \ddot{\theta}x &= -(1-\mu)\left[\frac{y}{d_{FS}^3} + y_L\left(\frac{1}{d_{FS}^3} - \frac{1}{d_{LS}^3}\right)\right] \\ &\quad - \mu\left[\frac{y}{d_{FE}^3} + y_L\left(\frac{1}{d_{FE}^3} - \frac{1}{d_{LE}^3}\right)\right] + f_{Fy} - f_{Ly}\end{aligned} \tag{7}$$

$$\begin{aligned}\ddot{z} &= -(1-\mu)\left[\frac{z}{d_{FS}^3} + z_L\left(\frac{1}{d_{FS}^3} - \frac{1}{d_{LS}^3}\right)\right] \\ &\quad - \mu\left[\frac{z}{d_{FE}^3} + z_L\left(\frac{1}{d_{FE}^3} - \frac{1}{d_{LE}^3}\right)\right] + f_{Fz} - f_{Lz}\end{aligned} \tag{8}$$

where

$$d_{LS} = \sqrt{(x_L + (1+\gamma)D)^2 + y_L^2 + z_L^2} \tag{9}$$

$$d_{LE} = \sqrt{(x_L + \gamma D)^2 + y_L^2 + z_L^2} \tag{10}$$

$$d_{FS} = \sqrt{(x + x_L + (1+\gamma)D)^2 + (y + y_L)^2 + (z + z_L)^2} \tag{11}$$

$$d_{FE} = \sqrt{(x + x_L + \gamma D)^2 + (y + y_L)^2 + (z + z_L)^2} \tag{12}$$

and $[f_{Lx} \quad f_{Lx} \quad f_{Lx}]^T$ and $[f_{Fx} \quad f_{Fx} \quad f_{Fx}]^T$ are the SRP force components acting on the leader and follower satellites, respectively.

B. Nonideal SRP Model

The description of the SRP model begins by defining the sail normal vector that is perpendicular to the sail surface and always points away from the sun. The sail normal $\hat{n}$ is specified by the two orientation angles ϕ and α (see Fig. 1) and is specified as

$$\hat{n} = \begin{bmatrix} \cos\alpha\cos\phi \\ \cos\alpha\sin\phi \\ \sin\alpha \end{bmatrix} \tag{13}$$

The optical coefficient set

$$\{\rho, s, \varepsilon_f, \varepsilon_b, B_f, B_b\} \tag{14}$$

parameterizes the nonperfectly reflecting behavior of the solar sail. These parameters are the reflection coefficient ρ, the specular reflection factor s, the front ε_f and backside ε_b emission coefficients, and the front B_f and backside B_b non-Lambertian coefficients. The nonperfectly reflecting solar sail model is expressed as [22]

$$\mathbf{F}_{\mathrm{SRP}} = \frac{\beta m(1-\mu)}{r_1^2}(\hat{r}_1 \cdot \hat{n})\{b_1\hat{r}_1 + [b_2(\hat{r}_1 \cdot \hat{n}) + b_3]\hat{n}\} \tag{15}$$

where the optical coefficients are given by

$$b_1 = \tfrac{1}{2}(1 - s\rho) \tag{16}$$

$$b_2 = s\rho \tag{17}$$

$$b_3 = \frac{1}{2}\left[B_f(1-s)\rho + (1-\rho)\frac{\varepsilon_f B_f - \varepsilon_b B_b}{\varepsilon_f + \varepsilon_b}\right] \tag{18}$$

The solar sail lightness number is [11]

$$\beta = \frac{2p_0}{\mu_s}\frac{A_0}{m} \tag{19}$$

where the nominal SRP force is $p_0 = 1.04 \times 10^{17}$ N, μ_s is the solar gravitational parameter, A_0 is the sail reference area, and m is the satellite mass.

The optical parameters given in Eq. (14) are not expected to remain constant over course of the satellite mission. The degradation of the optical coefficients depends upon the solar radiation dose Σ that is received by the sail. The degradation constant λ is related to the half-life solar radiation dose $\hat{\Sigma}$ by $\lambda = \ln(2)/\hat{\Sigma}$. To simplify the degradation model, a single degradation factor d and a single half-life solar radiation dose is used for all of the optical parameters. The reflectivity of the sail decreases with time, whereas the emissivity increases with time. Therefore,

$$\begin{aligned}\rho_\infty &= \frac{\rho_0}{1+d} & s_\infty &= \frac{s_0}{1+d} & \varepsilon_{f\infty} &= (1+d)\varepsilon_{f0} \\ \varepsilon_{b\infty} &= \varepsilon_{b0} & B_{f\infty} &= B_{f0} & B_{b\infty} &= B_{b0}\end{aligned} \tag{20}$$

The degradation of the optical parameters in dimensionless form is given by

$$\frac{p(t)}{p_0} = \begin{cases} (1 + de^{-\lambda\Sigma(t)})/(1+d) & \text{for } p \in \{\rho, s\} \\ 1 + d(1 - e^{-\lambda\Sigma(t)}) & \text{for } p = \varepsilon_f \\ 1 & \text{for } p \in \{\varepsilon_b, B_f, B_b\} \end{cases} \tag{21}$$

C. SRP Effect on Libration Point Location

Consider the dynamics of one satellite in the CR3BP with the sail orientation angles set to zero. This configuration has the solar sail normal in line with the sun vector. Then the dynamic equations are

$$\ddot{x} - 2\dot{y} - x = -\frac{(1-\mu)(1-b_T\beta)(x+\mu)}{r_1^3} - \frac{\mu(x-(1-\mu))}{r_2^3} \tag{22}$$

$$\ddot{y} + 2\dot{x} - y = -\frac{(1-\mu)y}{r_1^3} - \frac{\mu y}{r_2^3}\ddot{z} = -\frac{(1-\mu)z}{r_1^3} - \frac{\mu z}{r_2^3} \tag{23}$$

$$\ddot{z} = -\frac{(1-\mu)z}{r_1^3} - \frac{\mu z}{r_2^3} \tag{24}$$

where $b_t = b_1 + b_2 + b_3$. The location of the collinear libration point along the $\hat{x}$ axis is found by solving the scalar equation

$$x - \frac{(1-\mu)(1-b_T\beta)(x+\mu)}{r_1^3} - \frac{\mu(x-(1-\mu))}{r_2^3} = 0 \tag{25}$$

Designating x_e as the distance from the system mass center to L_2 gives $\gamma = x_e - (1-\mu)$. Increasing the solar sail surface area has the effect of shifting the location of L_2 sunward.

D. Leader Spacecraft Reference Trajectory

The follower spacecraft dynamics, as shown in Eqs. (6–8), are dependant upon the trajectory of the leader spacecraft. In this study, a quasi-periodic halo trajectory at L_2 is specified in the ER3BP, which includes the effects of solar radiation pressure, using the two level differential correction method developed by Pernicka and Howell [23]. Although this method was originally developed for the determination of Lissajous trajectories in CR3BP, it can be used to transition solutions from the CR3BP model to the ER3BP model with only small variations in the trajectory shape. The reference trajectory developed in this study is not precisely periodic; however, the shape and size will satisfy L_2 mission requirements in which a halo orbit is required. The differential correction technique is not self starting and requires an initial approximation of the solution. Richardson [24] used the method of Lindstedt–Poincaré to develop a third-order solution for periodic motion about the collinear libration points. A modified form of this analytical solution that includes the effects of solar radiation pressure, as presented by McInnes [25], is used as the starting point for the determination of the leader reference trajectory in the ER3BP.

The differential corrections method uses trajectory arc segments that are patched together to form a continuous path. The startup solution is first decomposed into a series of segments and nodes. The first level corrector adjusts the velocities at all of the node points such that positional continuity is achieved across all of the trajectory segments. However, this results in velocity discontinuities (Δv) at the node points. The second level corrector adjusts the positions and segment times to reduce the Δv. Trajectory segments are then specified at the new node locations. The process is repeated until all of the Δv are below a specified threshold, giving a trajectory that is essentially continuous both position and velocity. The reader is referred to the work of Pernicka and Howell [23] for further details regarding this algorithm.

Because of the nonautonomous nature of the ER3BP, the reference trajectory is specific to the starting location of the Earth/moon system about the sun used in the calculation. In this study, a reference epoch of Julian date (JD) 2455566.8856746 (5 January 2011, 09:15:21 hrs) is used that corresponds to the Earth/moon system being at perihelion in its orbit about the sun. A reference trajectory spanning five years is developed and initial segment lengths are chosen to be 0.25 nondimensional time units in length. This requires 130 trajectory segments to be patched together. The largest velocity discontinuity over all of the nodes in the final trajectory is 1.4×10^{-7} m/s. Figure 2 shows the resultant leader spacecraft reference trajectory.

E. Follower Spacecraft Reference Trajectory

The configuration of the spacecraft formation is directly related to the scientific objectives of the mission. While it may be possible to

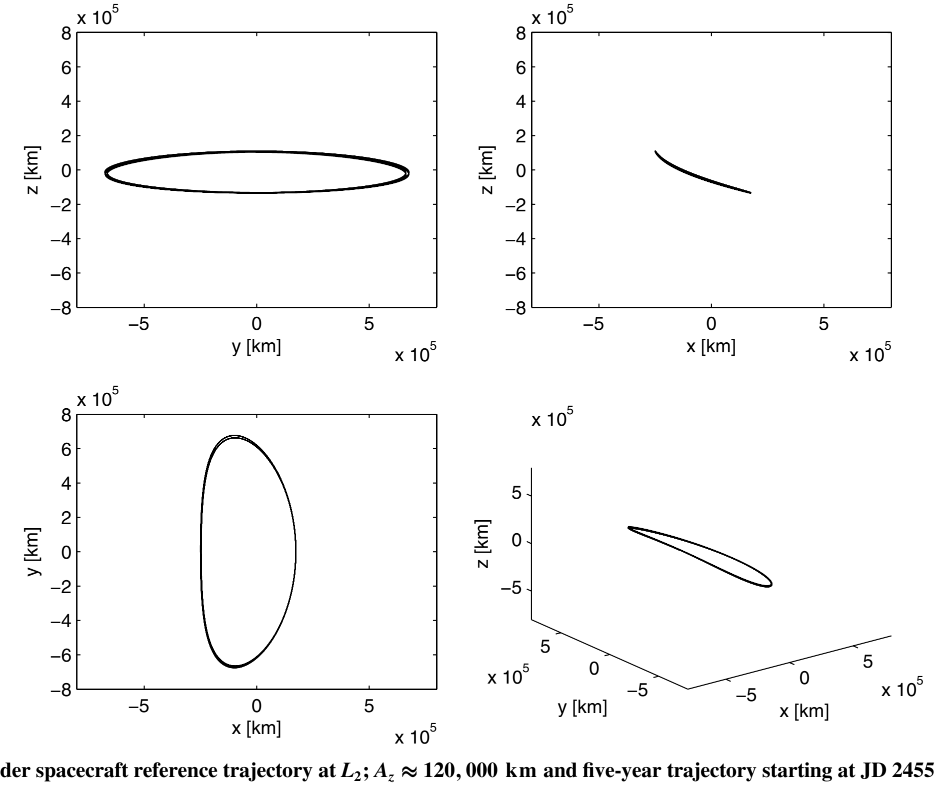

Fig. 2 Leader spacecraft reference trajectory at L_2; $A_z \approx 120,000$ km and five-year trajectory starting at JD 2455566.8856746.

use natural motions as candidate trajectories for some applications, in general, nonnatural formations will be needed to fulfill the mission goals. In the present investigation, we propose two formation trajectories that are suitable for upcoming L_2 spacecraft formation missions. First, a yz plane circular projected orbit in the L_2 is developed. Then an inertially oriented circular formation is presented that is suitable for astronomical observations. Both of these trajectories are based on the solution of the linearized equations of motion for SFF in the CR3BP. Segerman and Zedd [26] showed that the linearized L_2 SFF equations are the same form as the linearized equations for the motion of a single spacecraft about L_2. Therefore, the linearization of Eqs. (22–24) gives

$$\dot{X} = \begin{bmatrix} \dot{x} \\ \dot{y} \\ \dot{z} \\ \ddot{x} \\ \ddot{y} \\ \ddot{z} \end{bmatrix} = \begin{bmatrix} 0 & 0 & 0 & 1 & 0 & 0 \\ 0 & 0 & 0 & 0 & 1 & 0 \\ 0 & 0 & 0 & 0 & 0 & 1 \\ 1+2C_{L_2} & 0 & 0 & 0 & 2 & 0 \\ 0 & 1-C_{L_2} & 0 & -2 & 0 & 0 \\ 0 & 0 & -C_{L_2} & 0 & 0 & 0 \end{bmatrix} \begin{bmatrix} x \\ y \\ z \\ \dot{x} \\ \dot{y} \\ \dot{z} \end{bmatrix} \tag{26}$$

where the linearization constant is given by

$$C_{L_2} = \frac{1-\mu}{(1+\gamma)^3} + \frac{\mu}{\gamma^3} \tag{27}$$

The in-plane and out-of-plane eigenvalues (frequencies) are given by

$$\nu_{xy} = \sqrt{-\frac{C_{L_2}}{2} + 1 + \frac{1}{2}\sqrt{9C_{L_2}^2 - 8C_{L_2}}} \tag{28}$$

$$\nu_z = \sqrt{C_{L_2}} \tag{29}$$

and the constant that relates the x and y amplitudes is

$$k = \frac{\nu_z^2 + 1 + 2C_{L_2}}{2\nu_z} \tag{30}$$

The ratio ν_{xy}/ν_z is nonrational resulting in a quasi-periodic motion about the libration point that is commonly referred to as a Lissajous trajectory. Defining A_x and A_z as the x and z amplitudes, and ψ_{xy} and ψ_z as the in-plane and out-of-plane phase angles, respectively, the Lissajous trajectory can be expressed as

$$\begin{bmatrix} x \\ y \\ z \end{bmatrix} = \begin{bmatrix} -A_x\cos(\nu_{xy}t + \psi_{xy}) \\ kA_x\sin(\nu_{xy}t + \psi_{xy}) \\ A_z\sin(\nu_z t + \psi_z) \end{bmatrix} \tag{31}$$

This trajectory is not particularly useful for any scientific missions involving sensing and observation, since the trajectory is nonperiodic and the orientation of the follower spacecraft is constantly changing. The Lissajous trajectory can be modified to form reference trajectories more suitable for space missions.

1. Local yz Circular Projected Trajectory

To produce a projected circular trajectory in the yz plane, the constraint $r_f^2 = y^2 + z^2$ needs to be satisfied, where r_f is the desired radius of the projected trajectory. To produce a periodic path, the out-of-plane frequency is set equal to the in-plane frequency and the amplitudes are adjusted. The resulting trajectory is

$$\begin{bmatrix} x_d \\ y_d \\ z_d \end{bmatrix} = r_f \begin{bmatrix} -\frac{1}{k}\cos(\nu_{xy}t + \psi) \\ \sin(\nu_{xy}t + \psi) \\ \cos(\nu_{xy}t + \psi) \end{bmatrix} \tag{32}$$

This type of trajectory is useful for missions studying the Earth from the sun–Earth/moon L_2 point. Note that the z phase angle has been shifted by 90 deg.

2. Inertially Fixed Circular Trajectory

Given a direction defined by azimuth angle φ and elevation angle ε in the sun–Earth/moon barycenter frame, an inertially fixed circular trajectory of radius r_f that points in this direction is given by

$$\mathbf{r}_I = \begin{bmatrix} \cos\varphi\cos\varepsilon & -\sin\varphi & -\cos\varphi\sin\varepsilon \\ \sin\varphi\cos\varepsilon & \cos\varphi & -\sin\varphi\sin\varepsilon \\ \sin\varepsilon & 0 & \cos\varepsilon \end{bmatrix} r_f \begin{bmatrix} 0 \\ \sin(\nu_{xy}t + \psi) \\ -\cos(\nu_{xy}t + \psi) \end{bmatrix} \tag{33}$$

The rotation matrix from the rotating L_2 frame to the inertial frame is

$$R_{L_2 I} = \begin{bmatrix} \cos\theta & \sin\theta & 0 \\ -\sin\theta & \cos\theta & 0 \\ 0 & 0 & 1 \end{bmatrix} \tag{34}$$

Therefore, the inertially fixed circular trajectory as expressed in the L_2 frame is $\mathbf{r} = R_{L_2 I}\mathbf{r}_I$. This trajectory is useful for space missions that require inertial pointing, such as those observing phenomena in deep space. A sample trajectory of this type of $r_f = 25$ km for a number of orbits is shown in Fig. 3.

III. Design of Control Laws

A. Control Law Development

In this section we present the method for developing nonlinear control algorithms for the SFF system. A higher-order sliding-mode control technique is used to drive the trajectory states of the nonlinear system onto a sliding manifold and maintain the system's states on the sliding surface. Once the system reaches the sliding plane, the behavior of the system reduces to lower order dynamics and is insensitive to plant uncertainties and external disturbances. Typically, higher-order sliding-mode control methods are used for affine control systems in order to remove chattering in the control signal u. In this study, we want to have a smooth u and $\dot{u}$. To accomplish this we use a boundary layer to provide for a smooth control input. The attitude system of the spacecraft benefits from a smooth angle and angular velocity profile. For control law design, some assumptions and simplifications were made. These include setting the eccentricity of the Earth–sun orbit to zero, simplifying the sun vector in the collinear frame to $\hat{s} = [1 \quad 0 \quad 0]^T$, fixing the orientation of the leader spacecraft $\alpha_L = 0$ and $\phi_L = 0$, assuming the leader and follower spacecraft are both equipped with solar sails having the same area to mass ratio, and simplifying the SRP model by assuming $s = 1$ and $\varepsilon_f B_f = \varepsilon_b B_b$. With these simplifications, the equations used for control law design are

$$\ddot{x} - 2\dot{y} - x = -(1-\mu)\left[\frac{x}{d_{FS}^3} + [x_L + (1+\gamma)]\left(\frac{1}{d_{FS}^3} - \frac{1}{d_{LS}^3}\right)\right] - \mu\left[\frac{x}{d_{FE}^3} + [x_L + \gamma]\left(\frac{1}{d_{FE}^3} - \frac{1}{d_{LE}^3}\right)\right] + g_x \tag{35}$$

$$\ddot{y} + 2\dot{x} - y = -(1-\mu)\left[\frac{y}{d_{FS}^3} + y_L\left(\frac{1}{d_{FS}^3} - \frac{1}{d_{LS}^3}\right)\right] - \mu\left[\frac{y}{d_{FE}^3} + y_L\left(\frac{1}{d_{FE}^3} - \frac{1}{d_{LE}^3}\right)\right] + g_y \tag{36}$$

$$\ddot{z} = -(1-\mu)\left[\frac{z}{d_{FS}^3} + z_L\left(\frac{1}{d_{FS}^3} - \frac{1}{d_{LS}^3}\right)\right] - \mu\left[\frac{z}{d_{FE}^3} + z_L\left(\frac{1}{d_{FE}^3} - \frac{1}{d_{LE}^3}\right)\right] + g_z \tag{37}$$

where

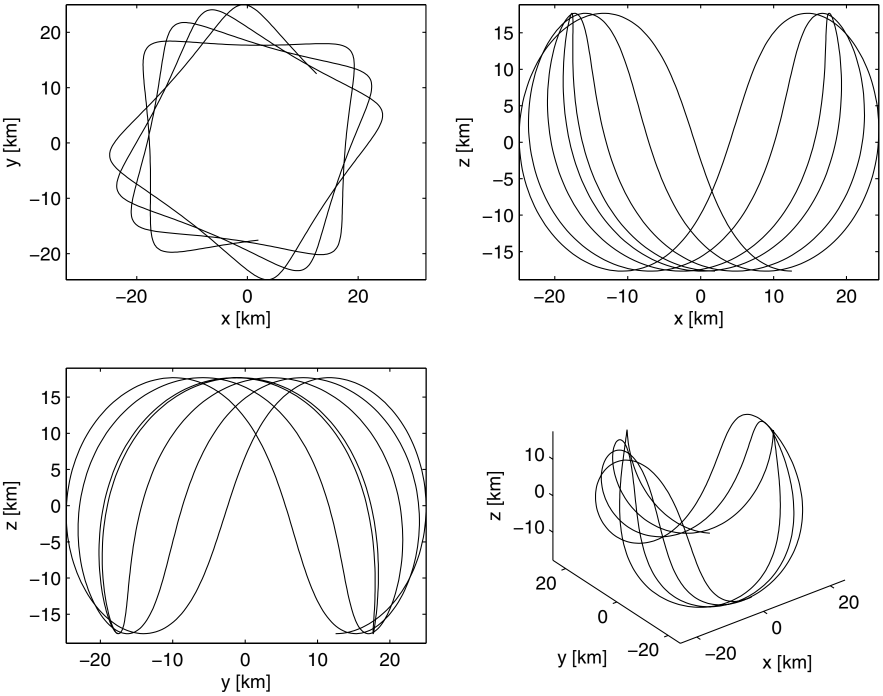

Fig. 3 Inertially fixed circular formation shown in local L_2 frame; $r_f = 25$ km, $\varphi = 45°$, $\varepsilon = 45°$, and $\psi = 0$.

$$g(u) = \begin{bmatrix} g_x \\ g_y \\ g_z \end{bmatrix} = \begin{bmatrix} (Q_0 + q)\cos^3\alpha\cos^3\phi - Q_0 \\ (Q_0 + q)\cos^3\alpha\cos^2\phi\sin\phi \\ (Q_0 + q)\cos^2\alpha\cos^2\phi\sin\alpha \end{bmatrix} \tag{38}$$

The control angles ϕ and α are augmented by an additional control input q that represents a change in the characteristic acceleration of the solar sail Q_0. From this value, the required change in sail surface area is determined. This control input is included in order to make the system fully actuated. Equation (35) can be written in simplified form as

$$\dot{X} = N(X) + Bg(u) \tag{39}$$

where $B = [0_{3\times 3} \quad I_{3\times 3}]^T$ and $g(u)$ is Eq. (38). The derivative of this equation is

$$\ddot{X} = \dot{N}(X) + BM\dot{u} \tag{40}$$

where

$$M = \begin{bmatrix} \frac{\partial g_x}{\partial q} & \frac{\partial g_x}{\partial \phi} & \frac{\partial g_x}{\partial \alpha} \\ \frac{\partial g_y}{\partial q} & \frac{\partial g_y}{\partial \phi} & \frac{\partial g_y}{\partial \alpha} \\ \frac{\partial g_z}{\partial q} & \frac{\partial g_z}{\partial \phi} & \frac{\partial g_z}{\partial \alpha} \end{bmatrix} \tag{41}$$

The output variable s is specified as $s = Ce$, where

$$C = \begin{bmatrix} k_1 & 0 & 0 & k_2 & 0 & 0 \\ 0 & k_3 & 0 & 0 & k_4 & 0 \\ 0 & 0 & k_5 & 0 & 0 & k_6 \end{bmatrix} \tag{42}$$

and $e = X - X_d$. The sliding manifold is specified as

$$\sigma = \dot{s} + \lambda s \tag{43}$$

The nonlinear control law capable of precise formationkeeping and reconfiguration is given by

$$\dot{u}(t) = \begin{bmatrix} \dot{q}(t) \\ \dot{\phi}(t) \\ \dot{\alpha}(t) \end{bmatrix} = -(CBM)^{-1}\left[\eta\frac{\sigma}{\|\sigma\| + \delta} + C\ddot{X}_d + \lambda\dot{s}\right] \tag{44}$$

The required control input is determined by integrating Eq. (44), that is $u = \int \dot{u}\,\mathrm{d}t$.

B. Stability Analysis

In this section, we show that the control law given by Eq. (44) guarantees global asymptotic stabilization of the relative states of the spacecraft.

Theorem: For the system model in Eqs. (6–8), if the sliding manifold is chosen as Eq. (43), the control law is defined as Eq. (44), then the system reaches the sliding surface in finite time for a sufficiently small $\delta > 0$.

Proof: Consider the candidate Lyapunov function

$$V(\sigma) = \tfrac{1}{2}\sigma^T\sigma \tag{45}$$

and its corresponding derivative

$$\dot{V}(\sigma) = \sigma^T\dot{\sigma} \tag{46}$$

$$\dot{V}(\sigma) = \sigma^T[\ddot{s} + \lambda\dot{s}] \tag{47}$$

$$\dot{V}(\sigma) = \sigma^T[C(\ddot{X} - \ddot{X}_d) + \lambda\dot{s}] \tag{48}$$

Substituting the nonlinear relative equations of motion from Eq. (40) and the control law from Eq. (44) gives

$$\dot{V}(\sigma) = \sigma^T\left[C\dot{N} - \eta\frac{\sigma}{\|\sigma\| + \delta}\right] \tag{49}$$

which can be expressed as

$$\dot{V}(\sigma) \le \|\sigma\|\left[\|C\|\|\dot{N}\| - \eta\frac{\|\sigma\|}{\|\sigma\| + \delta}\right] \tag{50}$$

The norm of the nonlinear terms is assumed to be upper bounded by a constant that can be expressed as $\|\dot{N}\| \le \eta\xi$. This allows the first derivative of $V(\sigma)$ to be expressed as

$$\dot{V}(\sigma) \le -\eta\|\sigma\|\left[-\|C\|\xi + \frac{\|\sigma\|}{\|\sigma\| + \delta}\right] \tag{51}$$

From Eq. (51) it is evident that if

$$-\|C\|\xi + \frac{\|\sigma\|}{\|\sigma\| + \delta} \geq 0 \tag{52}$$

then $\dot{V}(\sigma) \leq 0$. The condition in Eq. (51) is satisfied if

$$\|\sigma\| \geq \frac{\delta\xi}{\|C\|^{-1} - \xi} \tag{53}$$

This condition can also be expressed as

$$V(\sigma) > \frac{1}{2}\left(\frac{\delta\xi}{\|C\|^{-1} - \xi}\right)^2 = \epsilon_1 \tag{54}$$

It is evident that $\dot{V}(\sigma) \leq -\epsilon_2\sqrt{2V(\sigma)}$ for some $\epsilon_2 > 0$. This indicates that the sliding boundary layer is reached in finite time. When a small δ is chosen, then every trajectory will enter the region $V(\sigma) \leq \epsilon_1$ and will be ultimately bounded with respect to the boundary ϵ_1. Therefore, the control input given by Eq. (44) drives the trajectory toward a boundary layer surrounding the sliding manifold σ and the system states remain in this region. □

IV. Results and Discussion

To study the effectiveness of the developed HOSMC controller, the nonlinear Eqs. (6–8), the control inputs Eqs. (44), the reference trajectories Eq. (32) and (33), and initial conditions are numerically simulated. The integration is carried out using the International Mathematical and Statistical Library routine DDASPG based on Petzoid–Gear backward differentiation formula [27] method with a tolerance of 1×10^{-12}. The system parameters used in this study are listed in Table 1. The variations of D and θ are determined from the two body solution of the SEM system and the proper initial conditions are selected for this system so as to produce an eccentric orbit of 0.016704. The Earth/moon system is initially at perihelion at JD 2455566.8856746 (5 January 2011, 09:15:21 hrs). The control angles are also subject to the conditions $|\phi| < \pi/2$ and $|\alpha| < \pi/2$. The control parameters used for all cases are listed in Table 2. The performance of the proposed SRP L_2 formation control strategy is examined by considering several cases. First, the ability of the control scheme to handle large initial condition errors is presented. Next, formation maneuvering and formationkeeping are examined. The effect of optical degradation on formation control is then shown. Finally, some comments regarding the feasibility of the solar sail sizing are presented.

A. Initial Condition Errors

At the beginning of the formation-flying mission, the leader and follower spacecraft will separate from the launch vehicle, and attempt to reach their target orbits. There is no guarantee, due to any number of unforeseeable events, that the formation spacecraft will be given the exact initial states. The onboard control system needs to be able to contend with large relative initial state errors. The ability of HOSMC to contend with these large initial errors is first presented. The system trajectories due to large initial state errors are shown in Fig. 4 and the corresponding system responses are shown in Fig. 5. Four different initial position errors are presented to demonstrate the ability of the proposed controller to recover from these errors. The initial positions of the spacecraft along with the corresponding phase angle of the reference yz circular projected formation is shown Table 3. The initial velocity for these cases is $[1.1\dot{x}_0 \quad 1.1\dot{y}_0 \quad 1.1\dot{z}_0]^T$. Despite the large initial errors, the maximum control effort required over all four cases is $|\Delta a|_{\max} = 10\ \text{m}^2$, $|\phi|_{\max} = 10°$, and $|\alpha|_{\max} = 5°$.

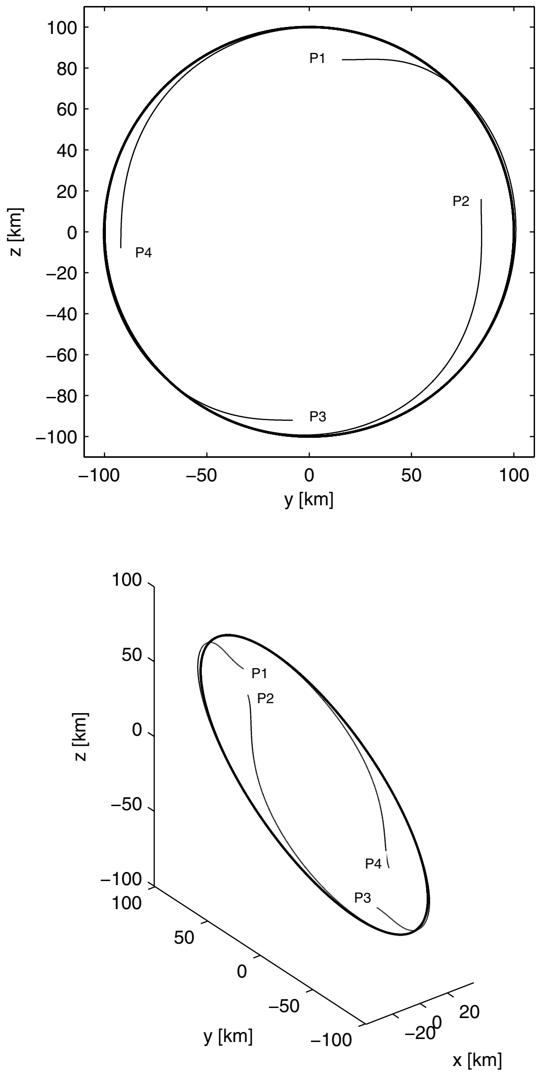

Fig. 4 System trajectory as affected by large initial state errors; *yz* circular projected trajectory $r_f = 100$ km.

Table 1 Reference system parameters

Parameter	Value
A_0	40, m^2
m	1000, kg
μ	3.0407×10^{-6}, nondimensional
γ	0.010072, nondimensional
ν_{xy}, ν_z	2.05838, 1.98647, nondimensional
k	3.18918, nondimensional
$\{\rho, s, \varepsilon_f, \varepsilon_b, B_f, B_b\}$	$\{0.88, 0.94, 0.05, 0.55, 0.79, 0.55\}$, nondimensional

Table 2 Control parameters

Parameter	Value
η_i, $(i = x, y, z)$	1000
λ_i, $(i = x, y, z)$	10
k_1, k_2	9.9819×10^6, 1.0010×10^5
k_3, k_4	3.1079×10^6, 3.3641×10^5
k_5, k_6	3.0973×10^6, 3.3610×10^5

Table 3 Initial conditions

Location	Position, km	Phase Angle ψ, deg
P_1	$[x_0 - 8 \quad y_0 + 16 \quad z_0 - 16]^T$	0
P_2	$[x_0 + 16 \quad y_0 - 16 \quad z_0 + 16]^T$	90
P_3	$[x_0 + 8 \quad y_0 - 8 \quad z_0 + 8]^T$	180
P_4	$[x_0 - 16 \quad y_0 + 8 \quad z_0 - 8]^T$	270

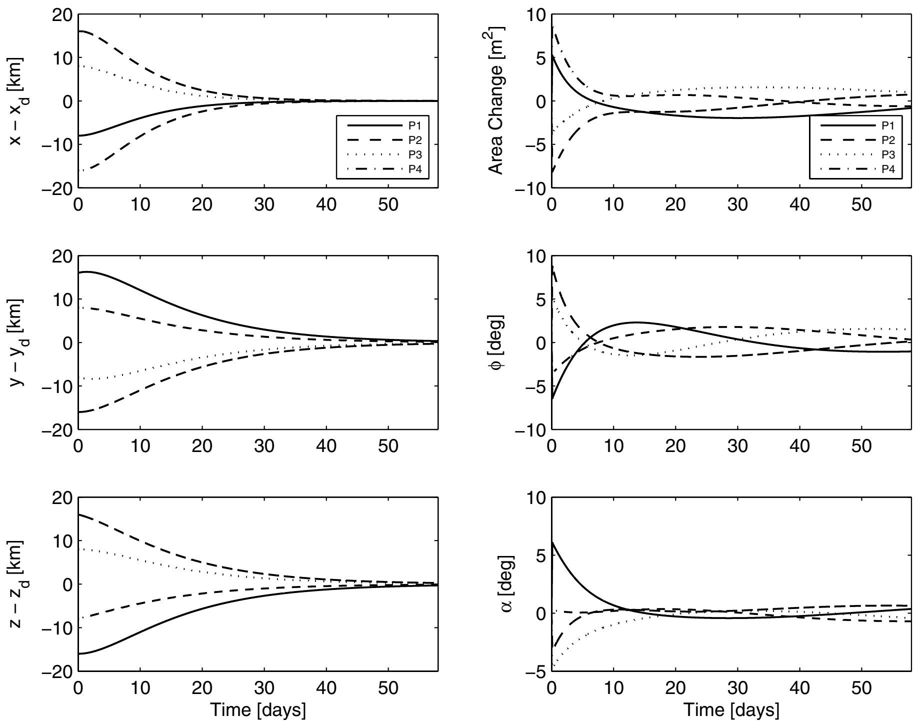

Fig. 5 System response as affected by large initial state errors; *yz* circular projected trajectory and $r_f = 100$ km.

B. Formation Reconfiguration and Formation Keeping

One of the main benefits of formation flying is the ability to reconfigure the spacecraft formation to achieve different mission objectives. In addition, a spacecraft in a formation cluster may fail, but the loss of a single follower spacecraft need not jeopardize the entire mission. Instead, the formation can be reconfigured by repositioning the remaining spacecraft allowing the mission to proceed unhindered. The proposed HOSMC strategy using SRP can be used for formation reconfiguration. In Fig. 6, the spacecraft is initially on a $r_f = 50$ km *yz* circular projected trajectory. A command is given at 200 and 400 days to increase the formation size by 25 km. Mission requirements may call for increasing the baseline between the leader and follower satellite. The tracking errors and control inputs needed to execute these maneuvers are shown in Fig. 7. For an inertially fixed formation, the ability to point the formation at a different celestial object is important. In Fig. 8, the formation has an initial size of $r_f = 20$ km and is pointing at the star Tania Boreilis ($\varphi = 150.28°$ and $\varepsilon = 42.91°$). At 175 days, the formation size is increased to $r_f = 40$ km and the direction changed to point at Kappa Leonis ($\varphi = 36.64°$ and $\varepsilon = 26.92°$). Finally, at 350 days, the formation size is again increased to $r_f = 60$ km and the orientation changed to point at Assellus Boreilis ($\varphi = 26.30°$

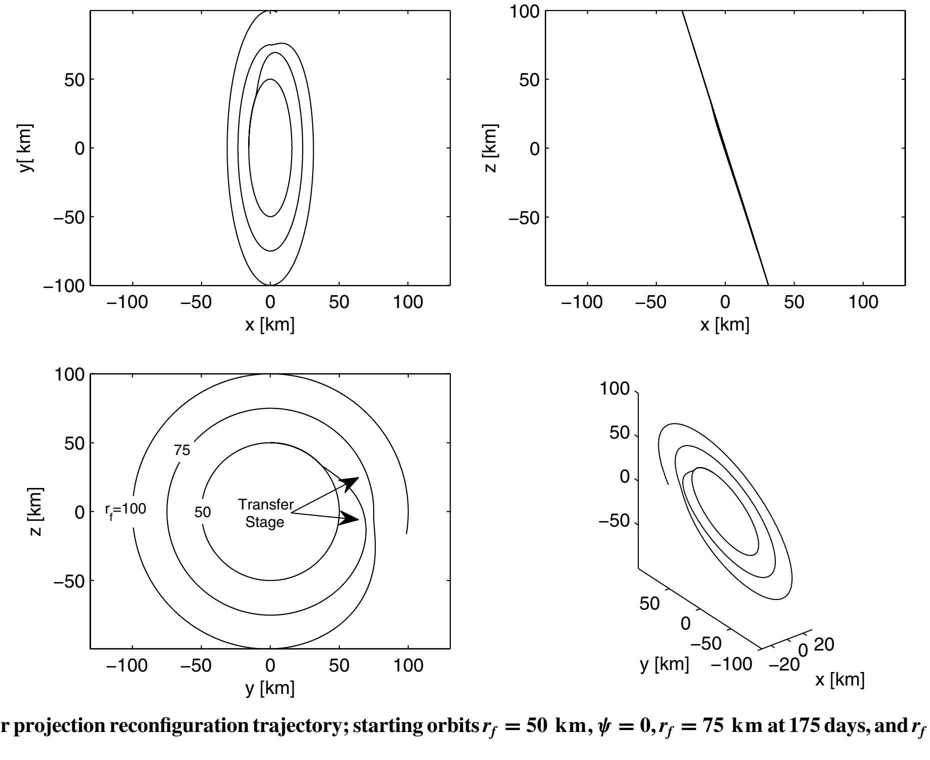

Fig. 6 Local *yz* circular projection reconfiguration trajectory; starting orbits $r_f = 50$ km, $\psi = 0$, $r_f = 75$ km at 175 days, and $r_f = 100$ km at 400 days.

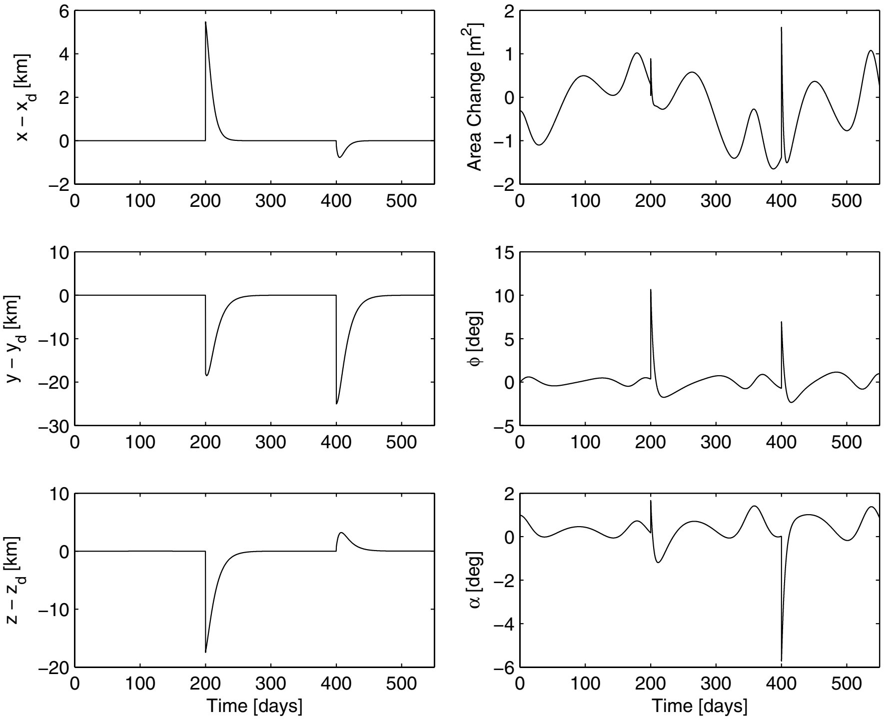

Fig. 7 Local *yz* circular projection system response; starting orbits $r_f = 50$ km and $\psi = 0$, $r_f = 75$ km at 175 days, and $r_f = 100$ km at 400 days.

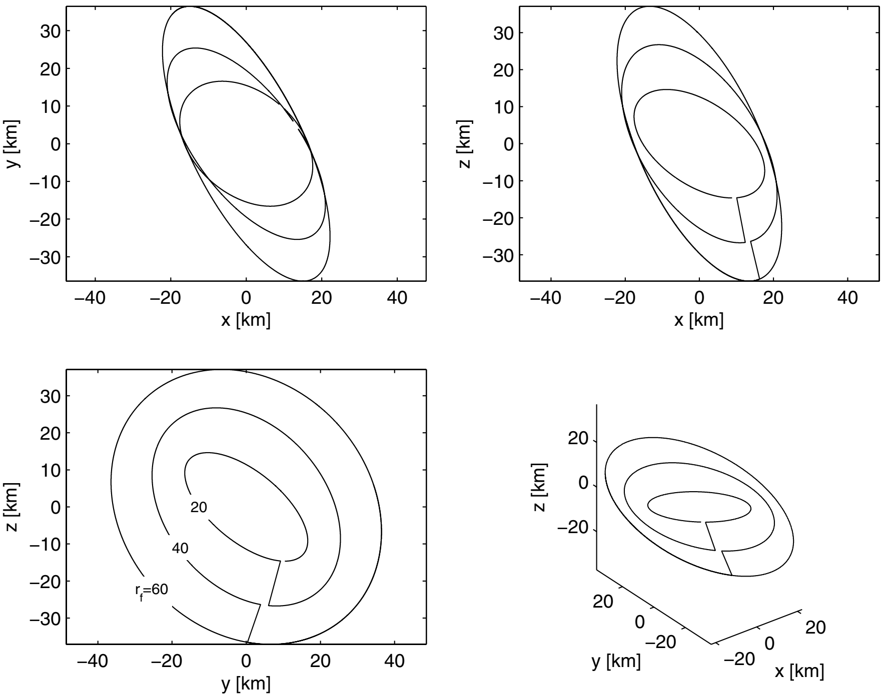

Fig. 8 Inertial circular formation reconfiguration trajectory; starting orbits $r_f = 20$ km, $\psi = 0$, $\varphi = 150.28°$, and $\varepsilon = 42.91°$; $r_f = 40$ km, $\varphi = 36.64°$, and $\varepsilon = 26.92°$ at 175 days; and $r_f = 60$ km, $\varphi = 26.30°$, and $\varepsilon = 21.90°$ at 350 days.

and $\varepsilon = 21.90°$). Figure 9 shows the tracking errors and control inputs needed for these reconfigurations. We have shown the ability of the proposed control technique to reconfigure the formation baseline and orientation.

The purpose of formationkeeping is to reduce the tracking errors and keep the follower spacecraft on the desired trajectory. Orbits about the collinear libration points are unstable, but controllable [21,28]. Therefore, active control is needed to maintain a desired formation. The formationkeeping cost of a 50 km yz circular projected trajectory is shown in Fig. 10 and a inertial 25 km circular formation ($\varphi = 45°$, $\varepsilon = 45°$) is shown in Fig. 11. In both cases, there is an initial small growth in the tracking error. Recall that the control inputs are obtained by determining $\dot{u}$ from Eq. (44) and integrating to obtain u. The initial values of the control inputs are taken to be (0, 0, 0). Because of this, a small initial drift occurs. In both cases the tracking error is less than 1 m.

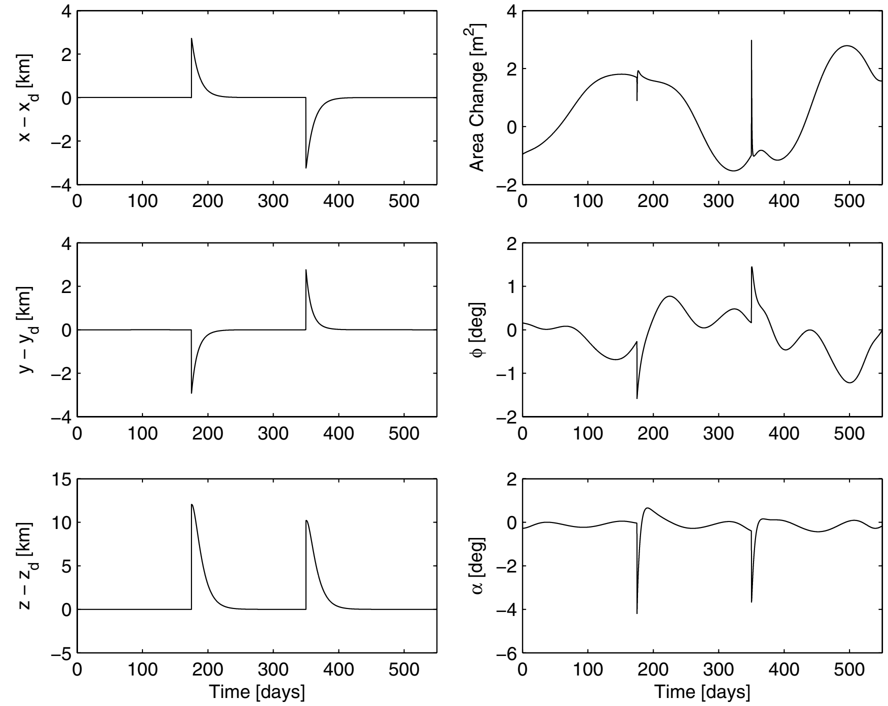

Fig. 9 **Inertial circular formation reconfiguration system response, starting orbits $r_f = 20$ km, $\psi = 0$, $\varphi = 150.28°$, and $\varepsilon = 42.91°$; $r_f = 40$ km, $\varphi = 36.64°$, and $\varepsilon = 26.92°$ at 175 days; and $r_f = 60$ km, $\varphi = 26.30°$, and $\varepsilon = 21.90°$ at 350 days.**

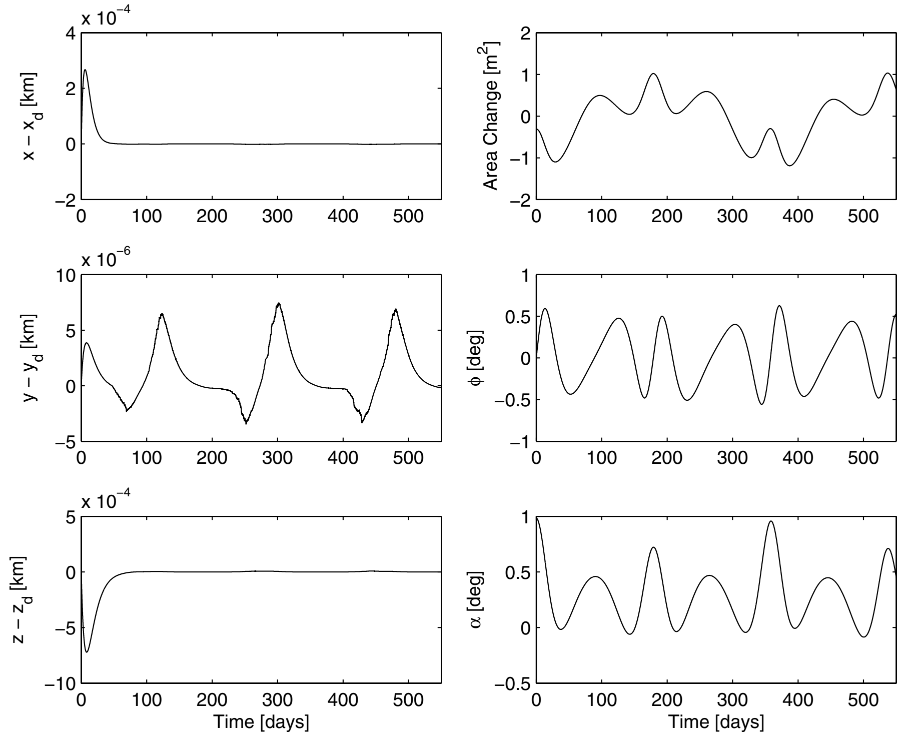

Fig. 10 **Local *yz* circular projected formationkeeping system response; $r_f = 50$ km and $\psi = 0$.**

C. Solar Sail Optical Degradation

The effect of optical degradation of the solar sail material needs to be considered when SRP is to be used for formation control at the collinear libration points. Equation (25) shows how the positions of the libration points are influenced by the presence of SRP. This influences the leader spacecraft. The follower spacecraft is affected by differential optical degradation rates of the leader and follower spacecraft. It is expected that the optical properties of solar sail materials will degrade due to the harsh space environment. However, the optical degradation rates of the leader and follower spacecraft are not expected to be the same. An extreme example of the effect of sail material degradation is shown in Fig. 12, where the leader spacecraft sail material does not degrade and the follower spacecraft sail surface has a degradation rate of $d = 0.2$. The tracking error remains small, but the effect of the degradation is most pronounced on the area change control input Δa. As the sail material degrades, the reduced

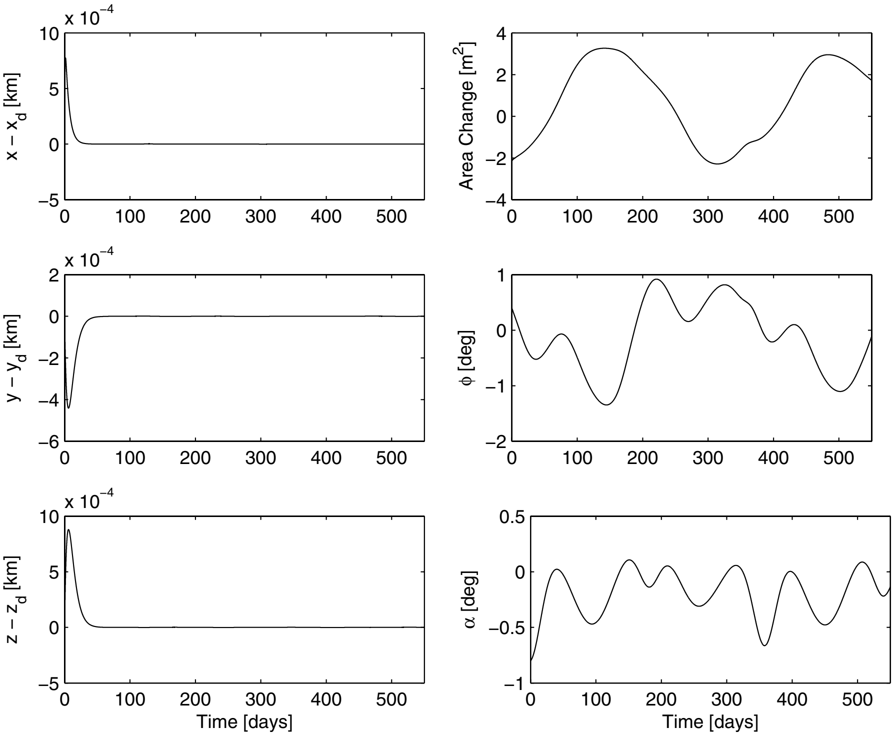

Fig. 11 Inertial circular formationkeeping system response; $r_f = 25$ km $\varphi = 45°$, $\varepsilon = 45°$, and $\psi = 0$.

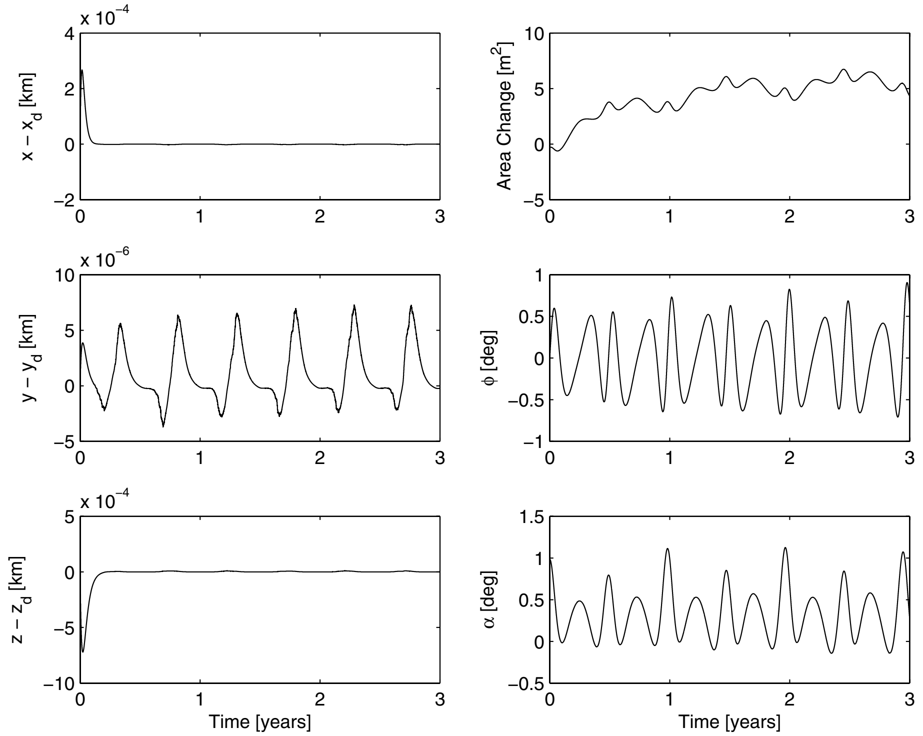

Fig. 12 Extreme optical degradation case; $d_L = 0, d_F = 0.2$, yz local circular projected formation, $r_f = 50$ km, and $\psi = 0$.

reflectivity is compensated for by increasing the sail surface area. The degradation effect on the control angles ϕ and α is small. The rates by which the leader and follower spacecraft optical properties degrade are not expected to be the same. This case is shown in Fig. 13, where the leader spacecraft has a moderate degradation rate of $d = 0.1$ and the follower spacecraft has rates above and below this value. Only Δa is shown in this plot, since the differential degradation effect is mostly noticed in the variation of this variable. Notice when the degradation rates are the same, no differential forces result. The increasing or decreasing control input due to optical degradation needs to be considered when designing a formation spacecraft system that uses SRP.

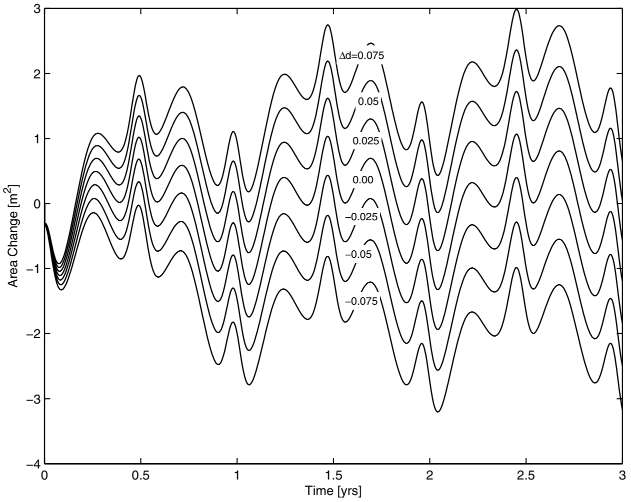

Fig. 13 Effect of differential optical degradation on area control input; $d_L = 0.1$, yz local circular projected formation, $r_f = 50$ km, and $\psi = 0$.

D. Solar Sail Sizing

Finally, we present some analysis regarding the feasibility of using a 40 m^2 solar sail for a 1000-kg-class spacecraft. The mass of the solar sail system on the spacecraft is composed of the solar sail material and the underlying support structure. The sail substrate constitutes the majority of the sail material mass. Kapton is one of the best substrate materials and has a surface density of 7.1 $\mathrm{g/m}^2$. The best choice of the surface coating is aluminum, which provides a reflectivity between 0.88 and 0.9 and has a surface density of 1.35 $\mathrm{g/m}^2$ [29]. Assuming a 50 m^2 surface area (40 m^2 is only the nominal value), the sail material will have a mass of 0.422 kg. To support the sail, a 20 m mast structure will be required that has a linear mass of 70 g/m [30], which totals 1.4 kg. Allowing for a few kilograms for the central hub mass and a 20% mass margin [29], the solar sail system has a mass of approximately 6 kg. Current solar sail technology has progressed to the point of successful ground based deployment of a 400 m^2 sail [31]. The size of the solar sail proposed in this study is reasonable given the state of current technology.

V. Conclusions

In this paper the use of solar radiation pressure for the control of a spacecraft formation-flying system located in the vicinity of the L_2 libration point was proposed. The system is composed of a leader and follower spacecraft. The two solar sail control angles augmented with an area control are considered as control inputs for controlling relative position of the follower spacecraft. The controller based on higher-order sliding-mode control was developed based on the nonlinear equations of motion to account for the nonaffine structure of the solar radiation pressure model control inputs. For control design, the CR3BP equations were used along with a simplified solar radiation pressure model. A control law that drives the system states to the sliding manifold, thereby forcing the plant to follow the desired reference trajectory was then formulated based on Lyapunov theory. The performance of the developed control law was tested on the ER3BP along with a nonideal solar radiation pressure model. Numerical results show that the proposed control method was able to maintain the desired formation. For the yz circular projected and inertial fixed circular formation trajectories used in this study, the tracking error was less than 1 m. Formation reconfiguration changes as high as 25 km required control input changes of 10 deg for the control angles and 4 m^2 for area change. The effect of the optical degradation of the solar sail material was investigated and was shown to mainly affect the area control input Δa. Overall, the numerical results establish the utility of solar radiation pressure for formation flying at the L_2 libration point.

References

[1] Lagadec, K., Lebas, J., and Ankersen, F., "Precision Formation Flying for the Darwin Interferometer," *5th ESA International Conference on Spacecraft Guidance, Navigation, and Control Systems*, ESA, Paris, 2002, pp. 201–207.

[2] Folta, D., Hartman, K., Howell, K., and Marchand, B., "The Stellar Imager (SI) Vision Mission," *Advances in Stellar Interferometry*, 2006, pp. 997–1014.

[3] Lawson, P., Lay, O., Martin, S., Peters, R., Gappinger, R., Ksendzov, A., et al., "Terrestrial Planet Finder Interferometer: 2007–2008 Progress and Plans," *Optical and Infrared Interferometry*, Vol. 7013, Marseille, France, 2008, Paper 70132N.

[4] Infeld, S., Josselyn, S., Murray, W., and Ross, I., "Design and Control of Libration Point Spacecraft Formations," *Journal of Guidance, Control, and Dynamics*, Vol. 30, No. 4, 2007, pp. 899–909. doi:10.2514/1.18654

[5] Pernicka, H., Carlson, B., and Balakrishnan, S., "Spacecraft Formation Flight about Libration Points Using Impulsive Maneuvering," *Journal of Guidance, Control, and Dynamics*, Vol. 29, No. 5, 2006, pp. 1122–1130. doi:10.2514/1.18813

[6] Marchand, B., and Howell, K., "Control Strategies for Formation Flight in the Vicinity of the Libration Points," *Journal of Guidance, Control, and Dynamics*, Vol. 28, No. 6, 2005, pp. 1210–1219. doi:10.2514/1.11016

[7] Wong, H., and Kapila, V., "Spacecraft Formation Flying near Sun-Earth L_2 Lagrange Point: Trajectory Generation and Adaptive Output Feedback Control," *American Control Conference*, June 2005, pp. 2411–2418.

[8] Luquette, R., and Sanner, R., "A Nonlinear Six Degree of Freedom Precision Formation Control Algorithm based on Restricted Three Body Dynamics," *Advances in the Astronautical Sciences*, Vol. 113, 2003, pp. 105–114.

[9] Gurfil, P., Idan, M., and Kasdin, N., "Adaptive Neural Control of Deep-Space Formation Flying," *Journal of Guidance, Control, and Dynamics*, Vol. 26, No. 3, 2003, pp. 491–501. doi:10.2514/2.5072

[10] McInnes, C., "Artificial Lagrange Points for a Partially Reflecting Flat Solar Sail," *Journal of Guidance, Control, and Dynamics*, Vol. 22, No. 1, 1999, pp. 185–187. doi:10.2514/2.7627

[11] Bookless, J., and McInnes, C., "Control of Lagrange Point Orbits Using Solar Sail Propulsion," *Acta Astronautica*, Vol. 62, No. 2, 2008, pp. 159–176. doi:10.1016/j.actaastro.2006.12.051

[12] Li, H., and Williams, T., "Reconfiguration of Sun-Earth Libration Point Formations Using Solar Radiation Pressure," *Journal of Spacecraft and Rockets*, Vol. 43, No. 6, 2006, pp. 1328–1339. doi:10.2514/1.16348

[13] Boskovic, J., Chen, L., and Mehra, R., "Adaptive Control Design for Nonaffine Models Arising in Flight Control," *Journal of Guidance, Control, and Dynamics*, Vol. 27, No. 2, 2004, pp. 209–217. doi:10.2514/1.1106

[14] Hovakimyan, N., Lavretsky, E., and Sasne, A., "Dynamic Inversion for Nonaffine-in-Control Systems via Time Scale Separation," *Journal of Dynamical and Control Systems*, Vol. 13, No. 4, 2007, pp. 451–464. doi:10.1007/s10883-007-9029-1

[15] Levant, A., "Sliding Order and Sliding Accuracy in Sliding Mode Control," *International Journal of Control*, Vol. 58, No. 6, 1993, pp. 1247–1263. doi:10.1080/00207179308923053

[16] Levant, A., Pridor, A., Gitizadeh, R., Yaesh, I., and Ben-Asher, J., "Aircraft Pitch Control via Second-Order Sliding Technique," *Journal of Guidance, Control, and Dynamics*, Vol. 23, No. 4, 2000, pp. 586–594. doi:10.2514/2.4591

[17] Bartolini, G., Ferrara, A., Usai, E., and Utkin, V., "On Multi-Input Chattering Free Second Order Sliding Mode Control," *IEEE Transactions on Automatic Control*, Vol. 45, No. 9, 2000, pp. 1711–1717. doi:10.1109/9.880629

[18] Galzi, D., and Shtessel, Y., "Formation Flight Strategy and Control Using Higher Order Sliding Mode," *AIAA Guidance Navigation and Control Conference*, Vol. 4, AIAA, Reston, VA, Aug. 2007, pp. 4100–4125.

[19] Shtessel, Y., Shkolnikov, I., and Levant, A., "Smooth Second Order Sliding Modes: Missile Guidance Application," *Automatica*, Vol. 43, 2007, pp. 1470–1476.

doi:10.1016/j.automatica.2007.01.008

[20] Kaveh, P., and Shtessel, Y., "Blood Glucose Regulation Using Higher Order Sliding Mode Control," *International Journal of Robust and Nonlinear Control*, Vol. 18, No. 4, 2008, pp. 557–569. doi:10.1002/rnc.1223

[21] Farquhar, R., "The Control and Use of Libration Point Satellites," Ph.D. Thesis, Stanford Univ., Department of Aeronautics and Astronautics, Stanford, CA, 1968.

[22] Dachwald, B., Seboldt, W., Macdonald, M., Mengali, G., Quarta, A. A., McInnes, C. R., et al., "Potential Solar Sail Degradation Effects on Trajectory and Attitude Control," *AIAA Guidance Navigation and Control Conference*, AIAA, Reston, VA, Aug. 2005, pp. 3274–3294.

[23] Pernicka, H., and Howell, K., "Numerical Determination of Lissajous Trajectories in the Restricted Three Body Problem," *Celestial Mechanics*, Vol. 41, No. 1, 1987, pp. 107–124. doi:10.1007/BF01238756

[24] Richardson, D., "Analytic Construction of Periodic Orbits About the Collinear Points," *Celestial Mechanics*, Vol. 22, 1980, pp. 241–253. doi:10.1007/BF01229511

[25] McInnes, A., "Strategies for Solar Sail Mission Design in the Circular Restricted Three-Body Problem," M.S. Thesis, Purdue Univ., West Lafayette, IN, 2000.

[26] Segerman, A., and Zedd, M., "Preliminary Planar Formation-Flight Dynamics Near Sun-Earth L_2 Point," *Advances in the Astronautical Sciences*, Vol. 114, 2003, pp. 507–526.

[27] International Mathematical and Statistical Library (IMSL), Software Package, Ver. 3.0, Visual Numerics, Inc., Houston, TX, 1997.

[28] Dunham, D., and Roberts, C., "Stationkeeping Techniques for Libration-Point Satellites," *Journal of the Astronautical Sciences*, Vol. 49, No. 1, 2001, pp. 127–144.

[29] McInnes, C., *Solar Sailing: Technology, Dynamics and Mission Applications*, Springer–Verlag, New York, 1999.

[30] Murphy, D., and Macy, B., "Demonstration of a 10 m Solar Sail System," *45th AIAA/ASME/ASCE/AHS/ASC Structures, Structural Dynamics and Material Conference*, Palm Springs, CA, 2004, pp. 698–708.

[31] Johnson, L., Young, R., and Montgomery, E., "Recent Advances in Solar Sail Propulsion Systems at NASA," *Acta Astronautica*, Vol. 61, 2007, pp. 376–382. doi:10.1016/j.actaastro.2007.01.047

C. McLaughlin
Associate Editor